La Matematica
https://doi.org/10.1007/s44007-024-00137-7

ORIGINAL RESEARCH ARTICLE

Analysis of Waveform Parameters in the Retinal Vasculature *via* Mathematical Modeling and Data Analytics Methods

Lorenzo Sala[1] · Kendall Lyons[2] · Giovanna Guidoboni[3] · Alon Harris[5] · Marcela Szopos[4] · Sergey Lapin[2]

Received: 2 February 2024 / Revised: 21 August 2024 / Accepted: 26 August 2024

Abstract

Patient-specific mathematical modeling combined with data analytics methods presents a promising approach for analyzing retinal hemodynamics. In this study, we build upon previous developments in retinal blood flow modeling, integrating clinical measurements and physiological insights to reconstruct parameters such as the central retinal artery velocity (CRA) Doppler profile and pressure wave. By leveraging personalized input data, including CRA velocity profile, systemic blood pressure, heart rate, and intraocular pressure, we evaluate the performance of our *in silico* approach. Our investigation highlights the significance of methodological considerations in combining automatic image processing and mathematical modeling, particularly concerning the selection of appropriate strategies and the inclusion of personalized supplementary data. Through extensive validation and comparison with prior works, we demonstrate the impact of different assessment methods on clinically meaningful quantities, particularly biomarkers related to blood flow. Furthermore, our study introduces a novel metric based on the Wasserstein distance for monitoring temporal changes in retinal blood flow dynamics, providing valuable insights into the evolution of vascular function. Overall, our findings underscore the importance of patient-specific input data, automatic image processing, and personalized mathematical modeling to ensure robust and clinically relevant outcomes in retinal vasculature analysis.

Keywords Mathematical ophthalmology · Image processing · Differential systems · Patient-specific modeling

✉ Lorenzo Sala
lorenzo.sala@inrae.fr

1 Université Paris-Saclay, INRAE, MaIAGE, 78350 Jouy-en-Josas, France

2 Department of Mathematics and Statistics, Washington State University, Pullman, WA, USA

3 Electrical and Computer Engineering, University of Maine, Orono, ME, USA

4 Université Paris Cité, CNRS, MAP5, 75006 Paris, France

5 Department of Ophthalmology, Icahn School of Medicine at Mount Sinai, New York, NY, USA

Published online: 11 September 2024

1 Introduction

The increasing interest in patient-specific mathematical models applied to biomedical challenges has propelled innovative research in recent years. Building upon clinical measurements and physiological insights, these models offer a promising avenue for understanding complex biological phenomena. This endeavor aligns with the evolving landscape of computational and mathematical ophthalmology, where innovative methodologies hold promise for enhancing diagnosis and monitoring of ocular diseases amidst a backdrop of diverse and sometimes conflicting clinical data [1, 2]. Contributions include the introduction, validation, and leveraging of models to analyze parameters such as the central retinal artery (CRA) velocity Doppler profile [3, 4] and pressure wave reconstruction. Alternative approaches, such as parametrizing the CRA pressure wave based on systemic blood pressure, heart rate, and incorporating intraocular pressure values, have significantly advanced our understanding of blood flow dynamics [5]. This strategic approach was extended to a more complex model for the lamina cribrosa, enabling virtual clinical studies [6], and has undergone extensive validation [7]. In parallel, computer-aided image processing studies, combined with statistical analysis [8, 9], identified novel patterns in the CRA velocity waveforms and parameters and correlated them with clinically significant biomarkers utilized in monitoring the glaucoma severity and progression. Such recent developments underscore the importance of comprehensive waveform analysis in elucidating vascular function and support their consideration as promising non-invasive clinical investigation tool for personalized research in ophthalmology.

Inspired by these recent advancements, our study aims to combine a previously validated physiologically-informed modeling strategy with the additional knowledge brought by using personalized CRA velocity waveforms as input data, in a unifying computational framework. Specifically, we seek to evaluate the performance of this data-driven modeling approach in comparison to prior works and, upon validation, extrapolate meaningful insights regarding other parts of the retinal vasculature that are not easily accessible with standard investigation methods, such as the central retinal vein (CRV) hemodynamics. By emphasizing the impact of different assessment methods on clinically meaningful quantities, our holistic approach could therefore contribute to the ongoing evolution of mathematical ophthalmology and provide valuable insights into the intricacies of retinal vascular dynamics.

The paper is organized as follows: a first section describes the methodology to automatically acquire from imaging data patient-specific CRA velocity waveforms (Sect. 2.1), the mathematical models employed to perform the simulations (Sect. 2.2) and the clinical and literature-based data incorporated in the model (Sect. 2.3). Then, Sect. 3 details the general framework of the numerical experiments setting. Results are presented and discussed in Sect. 4. Finally, conclusions and perspectives are outlined in Sect. 5.

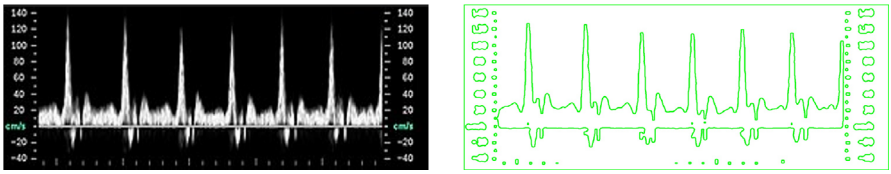

(a) Original profile image (b) Extracted profile image

Fig. 1 An example of the image manipulation process used to extract the central retinal vessels waveforms (right panel) from the original Doppler ultrasonography image (left panel)

2 Models and Methods

In this section we first present the methodology for semi-automatic digitalization of Doppler CRA velocity profiles, we describe the mathematical models representing the human retinal vasculature, and then we provide the details on the data employed in this study (clinical and literature-based).

2.1 Image Processing Algorithm for Waveform extraction

We utilize a variety of data analytics tools to develop a semi-automated algorithm for the examination of ocular blood flow and the extraction of velocity data from Doppler ultrasonography imaging. This algorithm is designed to identify waveform parameters, improve image quality, and capture specific data points.

In the pursuit of automatic extraction of waveform parameters from velocity profiles, a diverse array of Python libraries was employed with the primary goal of refining and analyzing ultrasound images. These libraries facilitated operations such as clarification, cropping, and edge detection on the initial ultrasound images. Such libraries are widely recognized for their utility in image analysis tasks, including edge detection and computer vision applications. Predominantly, the `OpenCV` [10] and `NumPy` [11] libraries were utilized for tasks involving image ingestion, cropping, and dimensional scaling. Within the confines of the current algorithm, the image undergoes an initial scaling to encapsulate both the graph and its corresponding units, followed by a conversion to a greyscale format. The conversion of the greyscale image to a binary format, delineating strictly black and white regions, represents the preliminary step in refining the data for subsequent edge analysis. Efforts to attenuate noise through the application of Gaussian and Median blur techniques [12] yielded comparable outcomes. Noteworthy advancements in edge detection were achieved utilizing the 'findContours' function inherent to the OpenCV library. Despite the merits of both approaches, the 'findContours' function was adjudged superior, owing to its simplicity in coding and the flexibility it offers in adjusting parameters such as the color and thickness of the resultant contours.

An illustrative example of the extraction process is provided in Fig. 1. Both CRA and CRV velocity waveforms are extracted, but due to the low quality of the CRV signal, we focused in the sequel on the information encapsulated in the CRA velocity waveform. The CRA velocity waveform was converted to a traditional XY coordinate

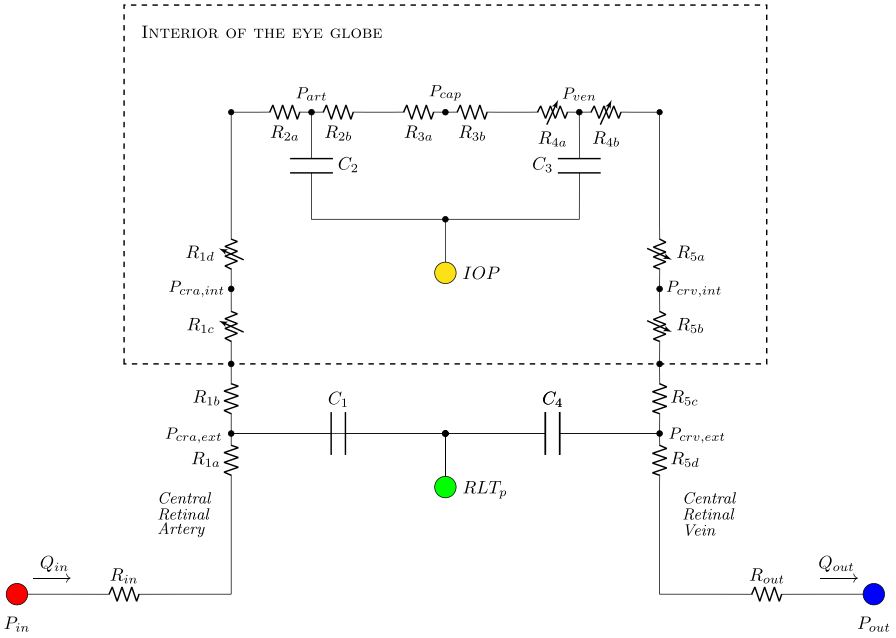

Fig. 2 Network model for the retinal vasculature. The dashed rectangle indicates the region corresponding to the interior of the eye globe. In this region, the variable resistors experience intraocular pressure (IOP) as external pressure, whereas in other parts of the circuit, the retrolaminar tissue pressure (RLTp) acts as external pressure

system using the web-based `WebPlotDigitizer` tool.[1] In `WebPlotDigitizer`, two points on the x-axis and y-axis must be identified to create the coordinate system. Then the user selects one cycle by means of the "BOX" tab under the "Automatic Extraction" section. All contours within this box will be delineated with a series of data points. The number of points identified can be altered by changing the pixel difference between points. Pixel differences can be altered in both the x and y dimensions to better fit the curve. The data is exported as a 1×2 matrix of time and velocity. Doppler profiles are often reported in cm/s.

2.2 Pressure and Blood Flow Computation from the Retina Model

Our study builds upon the model of the retinal vasculature introduced and validated in [13], as depicted in Fig. 2. This model partitions the vasculature into five primary compartments: CRA, arterioles, capillaries, venules, and CRV. Blood flow within this network is analogously conceptualized as electrical current traversing a circuit comprising resistors (R) and capacitors (C), where resistors represent vascular resistance and capacitors denote the vessel's ability to store blood volume. Each compartment and its segments are denoted by corresponding labels and further distinguished by alphabetic labels. Constant resistances are adopted for arterioles and capillaries since

[1] https://automeris.io/WebPlotDigitizer.

active changes in vascular diameters due to blood flow regulation are not accounted for in the present model. Three-element Windkessel models with constant resistances and capacitors are implemented to model the retrobulbar region of the CRA and CRV, subject to an external retrolaminar tissue pressure (RLTp). The expression for a generic constant resistance is:

$$R = \frac{k_r \rho \mathcal{L}}{\mathcal{A}^2}, \tag{1}$$

where $\mathcal{A}$ is the representative cross-sectional area of the compartment, $\mathcal{L}$ the representative compartment length, ρ is blood density, μ is blood dynamic viscosity and $k_r = 8\pi\mu/\rho$. In the case of a single vessel, $\mathcal{A}$ and $\mathcal{L}$ correspond to the vessel's cross-sectional area and length respectively.

The resistances of the translaminar and intraocular regions of CRA (R_{1c}, R_{1d}) and CRV (R_{5a}, R_{5b}), as well as the resistances in the venules segments (R_{4a}, R_{4b}) vary in response to IOP passively, expressing the mechanical response of the vessel wall to changes in transmural pressure. A hydrodynamic law describes the fluid flow through the network. In the case of arteries, Laplace's law [14] is used to model a pressurized cylindrical shell and Poiseuille's law is used to describe fluid flow through the vessel:

$$R = \frac{1}{k_0}\left[\frac{\hat{p} - p_e}{k_p\, k_L} + 1\right]^{-4} \tag{2}$$

with

$$k_0 = \frac{\mathcal{A}^2}{8\pi\mu\mathcal{L}}, \quad k_L = 12\frac{\mathcal{A}}{\pi h^2}, \quad k_p = \frac{E h^3 \pi^{3/2}}{12(1-\nu^2)\mathcal{A}^{3/2}}, \tag{3}$$

where h, E and ν are thickness, Young's modulus, and Poisson ratio of the vessel wall, respectively. The value of the transmural pressure $\hat{p} - p_e$ differs depending on the particular vascular segment under consideration: in the translaminar and intraocular regions, the pressure external to the vessel coincides with the intraocular pressure (IOP).

For the venous part, the transmural pressure difference may become negative, causing the vessel to collapse. This mechanism is modeled *via* the Starling resistor [14]:

$$R = \begin{cases} \dfrac{1}{k_0}\left[\dfrac{\hat{p} - p_e}{k_p\, k_L} + 1\right]^{-4} & \hat{p} \geq p_e \\ \dfrac{1}{k_0}\left[1 - \dfrac{\hat{p} - p_e}{k_p}\right]^{4/3} & \hat{p} < p_e \end{cases} \tag{4}$$

Note that in the original model, the external pressure on the vessel segments corresponding to resistances R_{1c} and R_{5b} was determined by a complex fluid–structure interaction model [15]. This pressure was derived from the effective stress exerted by the lamina cribrosa on these vessels. However, for the sake of simplicity in our study,

we assume that this stress has a similar order of magnitude as the stress deriving from the IOP as external pressure. This simplification allows us to clarify the modeling approach without significantly altering the outcomes of our investigation. Previous studies, such as those discussed in [5], have explored and confirmed the validity of such simplifications, indicating that our findings are not substantially affected by this assumption.

These conceptualizations are underpinned by Ohm's and Kirchoff's laws, leading to a system of ordinary differential equations governing pressure dynamics at the circuit nodes and flow rates within the retinal vasculature (5a)–(5b)–(5c)–(5d). Additionally, in this pressure-driven model, the inlet pressure (P_{in}) can fluctuate temporally across the cardiac cycle, further influencing the time-dependent nature of pressure calculations within the model.

$$\begin{cases} C_1 \dfrac{d(P_{cra,ext}-RLT_p)}{dt} = \dfrac{P_{in}-P_{cra,ext}}{R_{in}+R_{1a}} - \dfrac{P_{cra,ext}-P_{art}}{R_{1b}+R_{1c}+R_{1d}+R_{2a}} & \text{(5a)} \\ C_2 \dfrac{d(P_{art}-IOP)}{dt} = \dfrac{P_{cra,ext}-P_{art}}{R_{1b}+R_{1c}+R_{1d}+R_{2a}} - \dfrac{P_{art}-P_{ven}}{R_{2b}+R_{3a}+R_{3b}+R_{4a}} & \text{(5b)} \\ C_3 \dfrac{d(P_{ven}-IOP)}{dt} = \dfrac{P_{art}-P_{ven}}{R_{2b}+R_{3a}+R_{3b}+R_{4a}} - \dfrac{P_{ven}-P_{crv,ext}}{R_{4b}+R_{5a}+R_{5b}+R_{5c}} & \text{(5c)} \\ C_4 \dfrac{d(P_{crv,ext}-RLT_p)}{dt} = \dfrac{P_{ven}-P_{crv,ext}}{R_{4b}+R_{5a}+R_{5b}+R_{5c}} - \dfrac{P_{crv,ext}-P_{out}}{R_{5d}+R_{out}}. & \text{(5d)} \end{cases}$$

The time profile of the input pressure wave can be determined on a subject-specific basis using different methods. The first strategy is based on a parametrization of the reconstructed signal using the heart rate (HR), and the systemic systolic and diastolic pressures (SP and DP, respectively) as input from clinical data. The CRA blood pressure time profile is divided into 6 parts for each cardiac cycle and the pressure is explicitly computed according to the following formula:

$$P_{in}(t) = \begin{cases} 0.65\text{SP} - 0.475\text{DP}\,\sin\left(\dfrac{2\pi}{4\,0.082\,\frac{60}{\text{HR}}}\hat{t} + \dfrac{2\pi}{0.328\,\frac{60}{\text{HR}}}\,0.082\,\frac{60}{\text{HR}}\right) & \text{for } \hat{t} \le 0.082\,\frac{60}{\text{HR}} \\ 0.65\text{SP} + 0.9\,\sin\left(\dfrac{2\pi}{0.03\,\frac{60}{\text{HR}}}\hat{t} - \dfrac{2\pi}{0.03\,\frac{60}{\text{HR}}}0.082\,\frac{60}{\text{HR}}\right) & \text{for } 0.082\,\frac{60}{\text{HR}} < \hat{t} \le 0.112\,\frac{60}{\text{HR}} \\ 0.65\text{SP} + 0.118\text{SP}\,\sin\left(\dfrac{2\pi}{0.572\,\frac{60}{\text{HR}}}\hat{t} - \dfrac{2\pi}{0.572\,\frac{60}{\text{HR}}}\,0.112\,\frac{60}{\text{HR}}\right) & \text{for } 0.112\,\frac{60}{\text{HR}} < \hat{t} \le 0.398\,\frac{60}{\text{HR}} \\ -\dfrac{0.13\text{SP}}{0.034\,\frac{60}{\text{HR}}}\hat{t} + 0.65\text{SP} - \dfrac{0.13\text{SP}}{0.034\,\frac{60}{\text{HR}}}0.398\,\frac{60}{\text{HR}} & \text{for } 0.398\,\frac{60}{\text{HR}} < \hat{t} \le 0.432\,\frac{60}{\text{HR}} \\ 0.52\text{SP} - 0.8\,\sin\left(\dfrac{2\pi}{0.05\,\frac{60}{\text{HR}}}\hat{t} - \dfrac{2\pi}{0.05\,\frac{60}{\text{HR}}}\,0.332\,\frac{60}{\text{HR}}\right) & \text{for } 0.432\,\frac{60}{\text{HR}} < \hat{t} \le 0.482\,\frac{60}{\text{HR}} \\ 0.52\text{SP} + (0.52\text{SP} - 0.5\text{DP})\,\sin\left(\dfrac{2\pi}{2.072\,\frac{60}{\text{HR}}}\hat{t} + \dfrac{2\pi}{2.072\,\frac{60}{\text{HR}}}\,0.554\,\frac{60}{\text{HR}}\right) & \text{for } \hat{t} > 0.482\,\frac{60}{\text{HR}} \end{cases} \tag{6}$$

where $\hat{t} = \mod(t, \frac{60}{\text{HR}})$. Figure 3 displays the graph of P_{in} when using Eq. (6) and the baseline parameter values (IOP = 15 mmHg, HR = 60 beats/min, SP = 120 mmHg, DP = 80 mmHg).

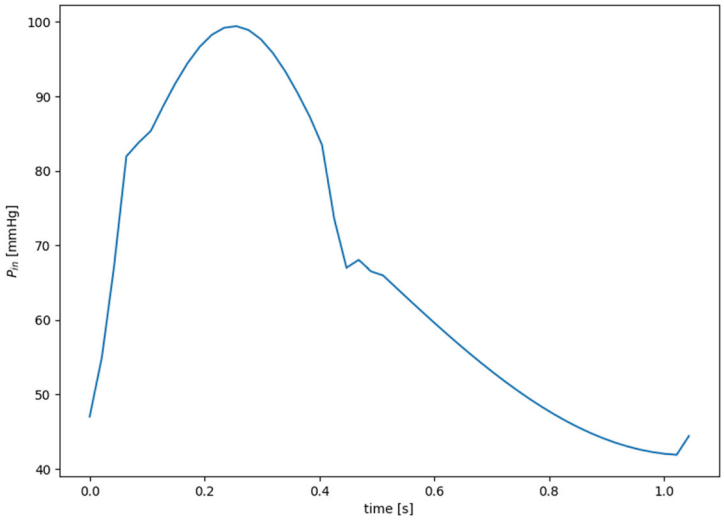

Fig. 3 Graph of P_{in} using Eq. (6) and baseline parameter values

Alternatively, Eq.(5a) can be re-written thanks to Poiseuille's law under the form:

$$C_1 \frac{d\left(P_{cra,ext} - RLT_p\right)}{dt} = Q_{in} - \frac{P_{cra,ext} - P_{art}}{R_{1b} + R_{1c} + R_{1d} + R_{2a}} \tag{7}$$

and in this case, the model is driven by the inlet flow Q_{in}. The inlet flow can be determined through a two-stage procedure: (i) the waveform extraction method of data from Doppler ultrasonography image measurements of blood velocity in the CRA, as explained in Sect. 2.1, followed by a processing step that computes the flow rate from the velocity values and the vessel diameter, here $D_{CRA} = 175\,\mu\text{m}$ [13] and (ii) the solving of (7)–(5b)–(5c)–(5d) taking as input data the flow rate instead of pressure.

As for the outlet pressure P_{out}, to mitigate the impact of the low quality of the CRV signal and the lack of information about its temporal dynamics, we choose to utilize for both pressure-driven and flow-driven models a constant baseline value of 14 mmHg, corresponding to a physiological order of magnitude downstream of the CRV [13]. In what concerns the values of the other parameters involved in the description of the retinal circuit at control state, details are provided in Sect. 3.

The numerical solving of the mathematical models previously described has been implemented in a Python in-house solver based on the `SciPy` [16] library, which can be openly shared upon request.

2.3 Clinical Data

In this section we provide details on clinical data and literature-based information that are incorporated into the models.

Table 1 Input data of the baseline and the five patients from IGPS

Patient	SP (mmHg)	DP (mmHg)	HR (beats/min)	IOP (mmHg)
Baseline	120	80	60	15
P1	125.73	78.27	76.91	20.27
P2	132.45	92.73	67.1	14.18
P3	120.2	72.2	88.6	11.89
P4	140.8	75.8	83.0	7.5
P5	129.5	83.7	56.4	15.91

The clinical data utilized here originate from the Indianapolis Glaucoma Progression Study (IGPS) [17] and from experimental data reported in [13]. The IGPS is a longitudinal study that aims to investigate the relationship between ocular hemodynamics and glaucoma progression. More precisely, 115 open-angle glaucoma patients were assessed every 6 months over a 7 year period. A rich set of data was acquired, among which IOP, SP, DP, HR, as well as structural and hemodynamic evaluations *via* multiple imaging devices [17, 18]. For the present pilot investigation, we extracted a subset of 5 patients (labeled hereafter P1, P2, P3, P4, P5) for whom we have access to their systemic condition (SP, DP, HR) as well as the value of IOP. Additionally, we retrieved the CRA blood flow velocity waveform measured by Doppler ultrasonography and derived quantities, with their raw values obtained directly from the device. Furthermore, we extracted and employed as baseline value the velocity waveform available in [13, Fig. 3, panel (b)], together with parameter information for a healthy subject (called in the sequel *Baseline*). Finally, for validation purposes, we consider results reported in [8] from a computer-aided analysis of CRA velocity waveforms.

3 Numerical Experiments Setting

We present in this section the general framework of the three sets of numerical experiments performed in this contribution. Specifically, we describe the list of subject-specific inputs that we include in the model and identify meaningful outputs of our analysis.

The first test case, numerical experiment A (Num. Exp. A) is using as inputs SP, DP, HR, and IOP values from the IGPS. These information are passed to the pressure-driven model, which exploits the parametrization in Eq. (6) for P_{in}. For the baseline patient we directly exploit data provided in [13] where SP/DP $=$ 120/80 mmHg, IOP $=$ 15 mmHg, and HR $=$ 60 beats/min. For the five IGPS patients, we computed the mean over the different visits of the clinically measured values of the considered inputs (SP, DP, IOP, HR) (see Table 1). For the second test case, numerical experiment B (Num. Exp. B), we employ the flow-driven model using as input the CRA flow waveform. The profile is reconstructed using the method presented in Sect. 2.1 for the five IGPS patients and for the baseline subject from Figure 3b of [13] as explained above. Note that as IOP we considered the baseline value for all patients ($IOP =$

15 mmHg). The third numerical experiment, Num. Exp. C, combines the personalized CRA flow waveforms and the personalized IOP values from the IGPS database as inputs of the flow-driven model. The CRA flow profile is retrieved as for Num. Exp. B for the baseline and the five IGPS patients. The patient-specific value of IOP is extracted from the IGPS, see Table 1, as in Num. Exp. A.

A summary of all the parameter values employed in this study is presented in Tables 2 and 3. Table 2 lists the model parameters that remain constant across all patients and numerical experiments, while Table 3 details the parameters that are specific to individual patients and experiments. Additionally, Table 4 reports the initial conditions of the ODE system for each patient and experiment.

The outputs considered in this study are the same for all the numerical experiments. The rationale behind these specific choices is two-fold: the information pertaining to CRA will be compared with raw data measured in the IGPS and values reported in [8] for validation purposes, while the computations describing pressures and flows in the CRV will enrich the predictive capabilities of the model. The simulations were run until reaching a periodic state and then output quantities were extracted from the last cardiac cycle. In particular, we focus on:

- the length of the cardiac cycle (Tcc);
- the CRA blood velocity and pressure time-dependent profile;
- the CRV blood velocity and pressure time-dependent profile;
- the CRA and the CRV resistivity indexes (RI);
- the CRA and the CRV systolic and diastolic perfusion pressures ($sysPP$, $dysPP$);
- the computed time-dependent resistances in the venules and in the intraocular CRV segments.

In particular, we introduce the following notations to identify specific moments in time during the last simulated cardiac cycle: ps as peak systole, and ed as end diastole. Thus, the resistivity index RI is computed as

$$RI = \frac{v_{ps} - v_{ed}}{v_{ps}} \tag{8}$$

where v_{ps} and v_{ed} are the velocities at peak systole and end diastole, respectively. The CRA and CRV perfusion pressures are computed as

$$CRAsysPP = CRAsys - IOP \qquad CRAdysPP = CRAdys - IOP \tag{9}$$

$$CRVsysPP = CRVsys - IOP \qquad CRVdysPP = CRVdys - IOP \tag{10}$$

where $CRAsys$, $CRVsys$, $CRAdys$, and $CRVdys$ are the CRA and CRV pressures at systole and diastole, respectively.

Finally, the overall workflow, which combines the mathematical modeling and the subject-specific data extraction process, is depicted in Fig. 4.

Table 2 Summary of the model parameters employed in the circuit model common to all numerical experiments

Name	Parameters	Values	Units	References
P_{out}	P	14.00	mmHg	[13]
RLTp	P	7.00	mmHg	[13]
R_{in}	R	$2.25 \cdot 10^4$	mmHg s cm^{-3}	[13]
R_{1a}, R_{1b}	R	$4.30 \cdot 10^3$	mmHg s cm^{-3}	[13]
R_{1c}	k_0	$5.115 \cdot 10^{-3}$	cm^3 mmHg^{-1} s^{-1}	[13]
	k_L	58.223	(–)	
	k_p	23.089	mmHg	
	p_e	IOP	mmHg	
R_{1d}	k_0	$1.023 \cdot 10^{-3}$	cm^3 mmHg^{-1} s^{-1}	[13]
	k_L	58.223	(–)	
	k_p	23.089	mmHg	
	p_e	IOP	mmHg	
R_{2a}, R_{2b}	R	$6.00 \cdot 10^3$	mmHg s cm^{-3}	[13]
R_{3a}, R_{3b}	R	$5.68 \cdot 10^3$	mmHg s cm^{-3}	[13]
R_{4a}, R_{4b}	k_0	$2.8 \cdot 10^{-3}$	cm^3 mmHg^{-1} s^{-1}	[13]
	k_L	$1.2 \cdot 10^3$	(–)	
	k_p	0.054	mmHg	
	p_e	IOP	mmHg	
R_{5a}	k_0	$3.24 \cdot 10^{-3}$	cm^3 mmHg^{-1} s^{-1}	[13]
	k_L	$1.48 \cdot 10^3$	(–)	
	k_p	0.359	mmHg	
	p_e	IOP	mmHg	
R_{5b}	k_0	$16.2 \cdot 10^{-3}$	cm^3 mmHg^{-1} s^{-1}	[13]
	k_L	$1.48 \cdot 10^3$	(–)	
	k_p	0.359	mmHg	
	p_e	IOP	mmHg	
R_{5c}, R_{5d}	R	$1.35 \cdot 10^3$	mmHg s cm^{-3}	[13]
R_{out}	R	$5.74 \cdot 10^3$	mmHg s cm^{-3}	[13]
C_1	C	$7.22 \cdot 10^{-7}$	cm^3 mmHg^{-1}	[13]
C_2	C	$7.53 \cdot 10^{-7}$	cm^3 mmHg^{-1}	[13]
C_3	C	$1.67 \cdot 10^{-5}$	cm^3 mmHg^{-1}	[13]
C_4	C	$1.07 \cdot 10^{-5}$	cm^3 mmHg^{-1}	[13]

In particular, we report the values of the parameters necessary for computing each resistance, according to Eqs. (1), (2) and (4)

Table 3 Summary of the model parameters employed in the circuit model specific to each patient (first column) and each numerical experiment (second column)

	NUM. EXP.	Input Source	IOP (mmHg)
Baseline	A	P_{in} using SP,DP, HR from Table 1	15
	B	Q_{in} from reconstructed waveform	15
	C	Q_{in} from reconstructed waveform	15
P1	A	P_{in} using SP,DP, HR from Table 1	20.27
	B	Q_{in} from reconstructed waveform	15
	C	Q_{in} from reconstructed waveform	20.27
P2	A	P_{in} using SP,DP, HR from Table 1	14.18
	B	Q_{in} from reconstructed waveform	15
	C	Q_{in} from reconstructed waveform	14.18
P3	A	P_{in} using SP,DP, HR from Table 1	11.89
	B	Q_{in} from reconstructed waveform	15
	C	Q_{in} from reconstructed waveform	11.89
P4	A	P_{in} using SP,DP, HR from Table 1	7.5
	B	Q_{in} from reconstructed waveform	15
	C	Q_{in} from reconstructed waveform	7.5
P5	A	P_{in} using SP,DP, HR from Table 1	15.91
	B	Q_{in} from reconstructed waveform	15
	C	Q_{in} from reconstructed waveform	15.91

Specifically we give the details for the input source and the value of the IOP employed

Table 4 Pressure initial conditions imposed at the ODE system (5a)–(5b)–(5c)–(5d) for each patient and each numerical experiment

[mmHg]	NUM. EXP.	$P_{cra,ext}$	P_{art}	P_{ven}	$P_{crv,ext}$
Baseline	A	43.598	35.69	21.87	18.93
	B	43.598	35.69	21.87	18.93
	C	43.598	35.69	21.87	18.93
P1	A	44.43	36.87	23.42	18.71
	B	43.598	35.69	21.87	18.93
	C	44.43	36.87	23.42	18.71
P2	A	43.46	35.497	21.75	18.96
	B	43.598	35.69	21.87	18.93
	C	43.46	35.497	21.75	18.96
P3	A	43.34	35.32	21.64	18.996
	B	43.598	35.69	21.87	18.93
	C	43.34	35.32	21.64	18.996
P4	A	43.08	34.96	21.42	19.06
	B	43.598	35.69	21.87	18.93
	C	43.08	34.96	21.42	19.06
P5	A	43.598	35.69	21.87	18.93
	B	43.598	35.69	21.87	18.93
	C	43.598	35.69	21.87	18.93

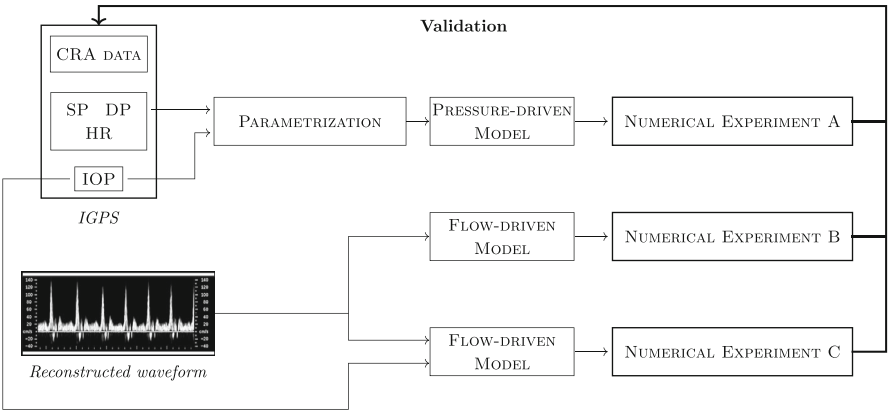

Fig. 4 Overview of the general workflow

4 Simulation Results

In this section, we report the findings of our combined methodology, divided in two parts. Section 4.1 focuses on a thorough validation process against experimental and literature data. Section 4.2 reports complementary results to assess the capabilities of the different methodological strategies and their impact on the output quantities of interest, as identified in the previous section.

4.1 Validation

Table 5 reports the validation of the numerical experiments performed in this study. Specifically we compute the CRA peak systolic velocity (*CRAvel ps*), the CRA end diastolic velocity (*CRAvel ed*), the CRA resistivity index (*CRA RI*—definition of RI in Eq. (8)), the time of the CRA peak systolic velocity within the last cardiac cycle (*CRAvel ps time*) and the length of a cardiac cycle (*Tcc*). The three numerical experiments are then compared with the clinical data reported in the IGPS [17] and with the finding of the computer-aided identification method for parameters characterizing the CRA waveform reported in [8].

For the NUM. EXP. A, we can evince that the CRA velocities are overestimated—with the exception of the *CRAvel ed* for patient P1, however, this fact is re-balanced in the computation of the *CRA RI* (the definition of RI is in Eq. (8)). The heart rate is directly imposed from the measured data, therefore the numerical experiment NUM. EXP. A and the IGPS data display the same values. As for *CRAvel ps*, the value computed for P4 (12.69 cm/s) is outside the range reported in literature (9.29 ± 2.54 cm/s). This fact could be explained looking at the high input blood pressures for this specific patient (Table 1). Using such pressures as only input of the model without the specific waveforms show the limitations of the NUM. EXP. A approach, where the CRA velocities are highly dependent on systemic blood pressure (see sensitivity analysis proposed in [5]), thus overestimated by the model for P4.

Table 5 CRA simulation results and comparison with experimental and literature data

	Baseline	P1	P2	P3	P4	P5
CRAvel ps (cm/s)						
Num. Exp. A	10.15	10.42	11.49	10.47	12.69	11.06
Num. Exp. B	10.00	9.95	7.89	10.05	7.73	9.74
Num. Exp. C	10.00	9.95	7.89	10.05	7.73	9.74
IGPS [17]		9.13	8.28	7.52	6.81	8.35
Carichino2020 [8]	9.29 ± 2.54					
CRAvel ed (cm/s)						
Num. Exp. A	2.89	2.40	2.96	2.30	2.49	3.09
Num. Exp. B	2.78	3.06	1.27	2.79	2.03	3.05
Num. Exp. C	2.78	3.06	1.27	2.79	2.03	3.05
IGPS [17]		2.68	2.53	1.95	2.19	2.61
Carichino2020 [8]	2.21 ± 0.78					
CRA RI						
Num. Exp. A	0.72	0.77	0.74	0.78	0.80	0.72
Num. Exp. B	0.72	0.69	0.84	0.72	0.74	0.69
Num. Exp. C	0.72	0.69	0.84	0.72	0.74	0.69
IGPS [17]		0.71	0.70	0.73	0.68	0.69
Carichino2020 [8]	0.75 ± 0.08					
CRAvel ps time (s)						
Num. Exp. A	0.24	0.17	0.21	0.15	0.16	0.25
Num. Exp. B	0.23	0.24	0.21	0.18	0.19	0.25
Num. Exp. C	0.23	0.24	0.21	0.18	0.19	0.25
IGPS [17]						
Carichino2020 [8]	0.15 ± 0.06					
Tcc (s)						
Num. Exp. A	1.00	0.78	0.89	0.68	0.72	1.06
Num. Exp. B	0.98	0.92	0.96	0.84	0.87	1.12
Num. Exp. C	0.98	0.92	0.96	0.84	0.87	1.12
IGPS [17]		0.78	0.89	0.68	0.72	1.06
Carichino2020 [8]	0.97 ± 0.15					

Underlined values are discussed in detail within the text

As for NUM. EXP. B and NUM. EXP. C, recall that we have the same values reported in the table since the reconstructed CRA velocity profile used as input of the numerical simulation is the same. On this basis, results show that the resistivity index is in very good agreement—with the exception of patient P2—between the reconstructed CRA velocity profile, the clinical measurements, and the literature data. In this case, also the HR may serve as validation of the input waveforms. Thus, we compared the length of the simulated cardiac cycles with the ones measured in the IGPS. The values are similar—even though slightly overestimated by the proposed *in silico* methodology.

Table 6 CRV simulation results

	NUM. EXP.	Baseline	P1	P2	P3	P4	P5
CRVvel ps (cm/s)	*A*	4.23	4.62	4.71	3.92	4.87	4.69
	B	4.24	4.09	3.12	3.88	2.96	3.98
	C	4.24	4.59	3.12	3.89	2.98	3.98
CRVvel ed (cm/s)	*A*	2.07	1.82	2.54	2.20	2.54	2.21
	B	2.04	2.28	1.36	2.44	1.61	2.15
	C	2.04	2.00	1.36	2.43	1.59	2.15
CRV RI	*A*	0.51	0.61	0.46	0.44	0.48	0.53
	B	0.52	0.44	0.56	0.37	0.46	0.46
	C	0.52	0.57	0.56	0.37	0.47	0.46

Underlined values are discussed in detail within the text

An important remark concerns *CRAvel ed* for all methodologies. The upper bound of the literature data is 2.99 cm/s, and for patients P1 and P5, the various numerical experiments slightly overestimate this value. We attribute this discrepancy to the poor accuracy of measurements for CRA at end diastole as stated also in [8], making them less reliable than measurements taken at peak systole.

Finally, for all three numerical experiments, Table 5 illustrates the values of the predicted time of the peak systole. These values are also in good agreement with the reported value in literature of 0.15 ± 0.06 s from the start of a cardiac cycle.

Overall, the computations suggest that, for all the methodologies proposed, the results are in good agreement with clinical measurements and other numerical experiments, capturing with satisfactory accuracy specific characteristics of both amplitude and accuracy of the signal. In addition, besides the clinical data in IGPS and data reported in [8], we compared our findings with the mean blood velocities in the CRA measured experimentally in [4, 19, 20], 6.25, 5.28 and 4.57 cm/s, respectively, equally in good accordance with our numerical outcomes.

4.2 Prediction

In this section we investigate the predictions made employing the three different strategies discussed in Sect. 3.

4.2.1 CRV

Table 6 gathers the simulation results concerning the CRV velocity as output.

We highlight that the measured IOP for these patients is quite high for patient P1 and below 16 mmHg for all the other patients (see Table 1), and therefore the model predictions should be interpreted in two different manners in this case. More precisely, for patient P1, the effect of having a personalized IOP measurement as an input seems to have a more substantial impact than the effect of having a personalized reconstructed CRA input velocity waveform; indeed, the values computed with NUM. EXP. A and NUM. EXP. C are very close, in contrast to the values obtained in the NUM. EXP.

B test case. For all the other patients the situation is the opposite. The CRV-related biomarkers are more influenced by the reconstructed input CRA velocity profile, than the use of a personalized IOP, as the results of NUM. EXP. B and NUM. EXP. C are in agreement between them and in contrast with the numerical solution for NUM. EXP. A test case. For the considered *Baseline* case, the IOP is exactly 15 mmHg, thus we do not have any difference between the NUM. EXP. B and the NUM. EXP. C test case.

4.2.2 Resistances in the Venous Side

We analyze now the effect of these changes in the variable resistances on the venous side (Table 7). For the purpose of presentation, we will focus on the computed values at peak systole and end diastole.

As expected, all the resistances are directly influenced by the value of IOP used, which explains the differences between NUM. EXP. B and NUM. EXP. C, but also the similarities between NUM. EXP. A and NUM. EXP. C. The most significant result is the very high value of CRV resistance for patient P1, which highlights the importance of having a personalized input IOP for patients suffering from ocular hypertension. Indeed, this clinical example shows how the high IOP affects the hemodynamics in the retina: specifically the model suggests a collapse in the CRV region. Note that the model is able to capture this behavior as a consequence of incorporating the Starling resistor effect, see Eq. (4), which is a crucial requirement to retrieve clinical data, as highlighted in [21]. Conversely, we point out patient P2. In this case, the effect of having a personalized CRA input waveform seems to have a greater impact on the resistances of the retinal venous system than the personalized IOP. Indeed the predicted values in the venules and in the CRV for NUM. EXP. B and NUM. EXP. C are very similar and remarkably higher than the values reported for NUM. EXP. A.

4.2.3 Retinal Perfusion Pressure

We now investigate the differences between the pressures within CRA and CRV and the IOP (Table 8) defined in Eq. (9).

It is noteworthy that the only case where this pressure is negative is for patient P1 which indeed suffers from high IOP. This table demonstrates once again how it is determinant to have both a personalized input blood velocity waveform and IOP value to detect abnormalities. This is especially significant on the CRV part, which is usually not accessible to clinical measurements, but which can be investigated thanks to the *in silico* modeling. We again took patients P1 and P2 as illustrative examples of distinct behavior:

- patient P1, as discussed, suffers from high IOP and this is clearly highlighted by the perfusion pressures in the CRV in the NUM. EXP. A test case. Using only the reconstructed CRA blood velocity profile (test case NUM. EXP. B), it is not possible to remark a deficit in the computed retinal hemodynamics, whereas clearly in both NUM. EXP. A and NUM. EXP. C the model identifies a collapsing behavior at the level of the veins (validated also by the values obtained in Table 7);

Table 7 CRV and venules resistances, simulation results

	Num. Exp.	Baseline	P1	P2	P3	P4	P5
Rven ps (mmHg s/mL)	*A*	2094.00	2544.51	1903.22	1863.00	1372.14	2073.20
	B	2089.99	2128.23	2397.11	2179.29	2443.32	2157.43
	C	2089.99	2586.86	2299.29	1872.68	1681.10	2256.24
Rven ed (mmHg s/mL)	*A*	2771.13	3265.31	2493.90	2316.16	1782.39	2852.15
	B	2784.85	2692.07	3066.88	2639.02	2954.43	2736.38
	C	2784.85	3148.84	2930.92	2246.59	1986.91	2872.52
Rcrv ps (mmHg s/mL)	*A*	295.82	306.27	292.37	290.11	277.79	296.22
	B	295.79	296.28	299.70	297.01	300.24	296.66
	C	295.79	306.36	297.87	290.21	283.94	298.69
Rcrv ed (mmHg s/mL)	*A*	303.42	7102.17	299.90	296.01	285.42	304.97
	B	303.53	302.65	305.96	302.10	305.07	303.14
	C	303.53	6409.11	304.10	295.21	288.58	305.20

Underlined values are discussed in detail within the text

Table 8 Retinal perfusion pressure, simulation results

	Num. Exp.	Baseline	P1	P2	P3	P4	P5
CRAsysPP (mmHg)	*A*	44.88	43.33	51.04	47.33	60.45	48.34
	B	44.28	44.09	35.04	41.83	33.83	43.26
	C	44.28	42.00	35.71	44.33	40.16	42.55
CRAdysPP (mmHg)	*A*	15.66	11.11	19.76	16.73	22.28	15.95
	B	15.19	17.89	8.35	17.65	11.57	17.27
	C	15.19	15.16	9.10	20.36	18.39	16.49
CRVsysPP (mmHg)	*A*	5.67	1.01	7.24	8.30	14.19	5.49
	B	5.68	5.45	3.91	5.12	3.67	5.28
	C	5.68	0.97	4.74	8.24	11.20	4.37
CRVdysPP (mmHg)	*A*	2.27	−3.41	3.83	5.58	10.51	1.58
	B	2.22	2.60	1.15	2.85	1.54	2.39
	C	2.22	−3.13	1.96	5.95	9.01	1.48

Underlined values are discussed in detail within the text

- simulation results for patient P2 suggest that when utilizing a personalized CRA input velocity, the computed values for the CRV perfusion pressure are notably lower compared to those predicted for the *Baseline* subject using the parameterized input pressure profile. This behavior may indicate a possible situation of risk, which has not been detected with the strategy adopted in Num. Exp. A.

Given the uncertainties in the measurement and the approximation in the mathematical model, it is impossible at this stage to select a threshold between a situation at risk of venous collapse. However, the different test cases display how the accuracy of effective biomarkers such as predicted retinal perfusion pressures might be increased by adding data to enrich personalized inputs.

4.2.4 CRA and CRV Waveforms

Finally, we explore the possibility of our simulations to predict clinical situations such as the risk of glaucoma. A first possibility would be to compare the obtained velocities within the CRA and the CRV two by two, as demonstrated for patients P1 and P3 in Fig. 5 for the Num. Exp. C. In this case, we observe that these two patients share similar hemodynamic conditions but have very different IOP values (see input values in Table 1). The outcome of this comparison shows that, thanks to the personalized inputs, we can distinguish between the similar CRA behavior (left panel) and the distinctly different CRV waveforms (right panel). Specifically, patient P1 exhibits lower velocity values in the CRV, which might indicate a risk of glaucoma [6]. However, this comparison process is very time-consuming. Therefore, we sought a metric that would be able to automatically consider the temporal evolution of CRA and CRV waveforms. In order to attempt this ambitious task we consider the blood pressure waveforms in the CRA and in the CRV computed in the three numerical experiments. Specifically, we compare the waveforms obtained for the healthy baseline

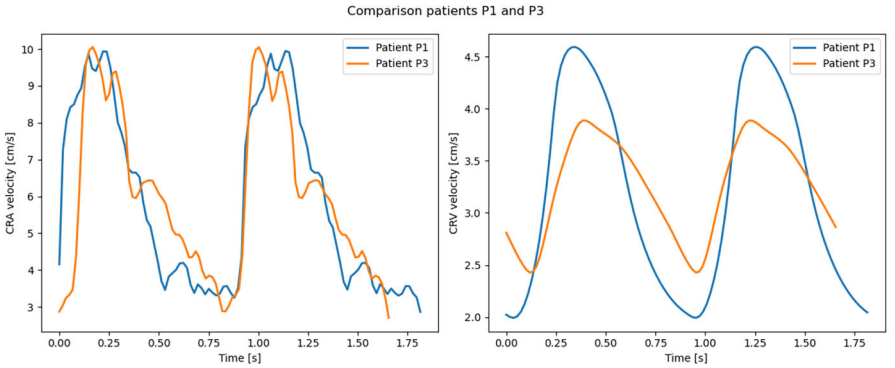

Fig. 5 Comparison of CRA and CRV velocity waveforms between patient P1 and patient P3 for Num. Exp. C

subject with the 5 predictions of the IGPS patients. Our proposal is to perform the comparison through the Wasserstein distance [22] (see Appendix A for more details), which quantifies the dissimilarity between two temporal sequences of blood pressure profiles. This refined metric has the advantage of taking into account not only the differences in the pressure values but also the temporal alignment of peaks, valleys, and overall shapes of the waveforms.

Table 9 presents the computed distances from the baseline for the five different subjects considered from IGPS. These values were compared to the reported IGPS measurements of the cup-to-disc area ratio, a well-known risk factor detected in glaucomatous patients [23, 24]. Through a preliminary analysis using Pearson's correlation coefficient, a strong correlation between the Wasserstein distance from the healthy baseline and the measured cup-to-disc area ratio was observed. Specifically, for the CRA, the correlation coefficient was 0.76 for Num. Exp. A, 0.91 for Num. Exp. B, and Num. Exp. C. Regarding the CRV, correlation coefficients of 0.81 for Num. Exp. A, 0.94 for Num. Exp. B, and 0.97 for Num. Exp. C were obtained. Despite the limitations imposed by the small sample size and the simplifying assumption in the reduced network-based modeling approach, these findings open the possibility to novel biomarkers exploiting temporal waveforms and underscore the predictive capacity of mathematical modeling. Notably, CRV waveforms, obtained numerically, exhibited all coefficients greater than 0.8. Furthermore, the utilization of personalized inputs, such as in Num. Exp. B and Num. Exp. C, yielded promising results (correlations $>= 0.9$).

5 Conclusions and Outlooks

In conclusion, our study underscores the significance of combining automatic image processing (Sect. 2.1) with mathematical modeling (Sect. 2.2) in the context of retinal vasculature and hemodynamic analysis. While this integration holds great promise, it is essential to exercise caution in selecting appropriate methodologies, as the choice can yield markedly different results as pointed out in Sect. 4.2. Such discrepancies

Table 9 Wasserstein distance from baseline for CRA and CRV blood pressure waveforms

	Num. Exp.	P1	P2	P3	P4	P5
CRA pressure distance from baseline (mmHg)	*A*	0.22	0.90	0.28	1.36	0.56
	B	0.36	1.50	0.68	1.54	0.55
	C	0.36	1.50	0.68	1.54	0.55
CRV pressure distance from baseline (mmHg)	*A*	0.27	0.48	0.12	0.63	0.29
	B	0.09	0.81	0.26	0.83	0.08
	C	0.24	0.81	0.26	0.83	0.09

may lead to substantial variations in clinical interpretation, particularly concerning metrics related to blood flow. Our findings emphasize the critical importance of rigorously evaluating and validating these methods to ensure their reliability and clinical relevance.

Furthermore, our investigation highlights the impact of supplementary data, in this specific case IOP, on the modeling outcomes. Comparing scenarios where IOP is considered as a baseline value versus as a personalized input, we observed varying effects on the modeling outcomes, particularly in specific regimes such as ocular hypertension. This underscores the importance of carefully considering the inclusion of supplementary data and its potential implications on modeling outcomes, especially in scenarios where personalized inputs may offer significant advantages over baseline assumptions.

As an additional outcome of our study, we assessed the potential of employing a novel metric, based on the Wasserstein distance, to monitor not only point-wise and classical values (e.g. quantities at peak systole and end diastole) but also the time evolution of parameters. This metric offers valuable insights into changes within the retinal vasculature over time, providing clinicians with enhanced tools for monitoring vascular function and potentially identifying early signs of pathology.

In summary, our study highlights the importance of methodological considerations in combining automatic image processing and mathematical modeling approaches, particularly in the context of retinal vasculature analysis. By critically evaluating different methodologies and supplementary data inputs, we can ensure more robust and clinically meaningful outcomes. Additionally, the development of a novel metric based on the time evolution of biomarkers offers exciting opportunities for advancing our understanding of vascular dynamics and improving clinical monitoring strategies.

This pilot work serves as a proof of concept for our cross-discipline approach of combining patient-specific clinical and imagery data with semi-autonomous mathematical modeling. This initial design was selected to serve as a test case for illustrating the novel methodologies and allow for small adjustments to enhance future applications within larger datasets. For example, one next step will be to improve rigor informed by these results by optimizing the image processing algorithm discussed in Sect. 2.1 to enable faster and more efficient handling of more robust datasets. Lack of patient diversity is another limitation of the current study. In the future we plan to extend the analysis to a larger number of patients and explore the potential integration of artificial intelligence techniques [25], inclusive of diverse samples across different ages, sex, race, and co-morbidities to increase the applicability of the models across populations. Leveraging these advanced computational approaches will allow us to further refine our mathematical framework and enhance our ability to analyze the results from a clinical perspective [26]. Through the application of machine learning algorithms combined with physics-based modeling, we aim to uncover hidden patterns, correlations, and predictive insights within the retinal vasculature data, ultimately contributing to more accurate diagnoses and personalized treatment strategies for ocular diseases.

A Wasserstein Distance

The Wasserstein distance, also known as the Earth Mover's Distance, is a metric used to quantify the distance between two probability distributions. Formally, it measures the minimum cost of transforming one probability distribution into another, where "cost" is defined in terms of a given ground distance between the elements of the distributions.

Given two one-dimensional probability mass functions, u and v, the classical Wasserstein distance between these two distributions is:

$$\mathcal{W}(u, v) := \inf_{\pi \in \Gamma(u,v)} \int_{\mathbb{R}\times\mathbb{R}} |x - y| d\pi(x, y). \tag{11}$$

In this context, $\Gamma(u, v)$ denotes the set of all joint probability distributions on $\mathbb{R} \times \mathbb{R}$ that have u and v as their marginal distributions. Essentially, for each value x, $u(x)$ indicates the probability associated with u at position x, and similarly, $v(x)$ indicates the probability associated with v at position x. The Wasserstein distance measures the minimum "cost" of transforming distribution u into distribution v, where the cost is defined as the distance $|x - y|$ for transporting probability mass from x to y.

The Wasserstein distance is a robust metric with several important properties and applications. As a true metric, it satisfies the fundamental properties of non-negativity, symmetry, and the triangle inequality, ensuring that the distance between distributions is always a non-negative value, the distance from one distribution to another is the same in either direction, and the distance between two distributions does not exceed the sum of their distances to a third distribution. Additionally, the Wasserstein distance is continuous with respect to the weak convergence of probability measures, meaning that as probability distributions converge weakly, their Wasserstein distance to a given distribution also converges. This continuity property makes it a reliable tool in statistical analysis. The versatility of the Wasserstein distance has led to its widespread use across various domains, including computer vision for tasks such as image retrieval and classification, machine learning for generative models and clustering, economics for measuring inequality and comparing income distributions, and fluid dynamics for tracking the evolution of fluid particles. Its ability to effectively compare distributions underpins its broad applicability and significance in these fields.

For our application we consider that u and v are two real-valued vectors of the same length, specifically the computed pressure waveforms lasting one cardiac cycle within the CRA and the CRV. In this case, the Wasserstein distance between their empirical distributions can be computed. This involves treating each element in the vectors as a discrete point with an equal probability mass. In practice, this means treating the elements of u and v as points in a metric space—here $\mathbb{R}$—and finding the optimal way to "move" the points of u to match the points of v. For our purpose we employed the library `scipy.stats` [16] in Python.

Unlike some metrics that only consider point-to-point differences, for instance the L^2 norm, the Wasserstein distance takes into account the overall shape and distribution of values in the time series. This makes it sensitive to the underlying distributions and robust to outliers. Additionally, by evaluating the entire distribution of values,

the Wasserstein distance can provide more stable and meaningful comparisons in the presence of noisy data. This is particularly important in contexts like clinical measurements, such as Doppler velocity measures.

Acknowledgements Professor Giovanna Guidoboni has been partially supported by NSF DMS 2108711/2327640 and NIH R01EY034718. Professor Alon Harris is supported by NIH grants (R01EY030851 and R01EY034718), NYEE Foundation grants, The Glaucoma Foundation grant, and in part by a Challenge Grant award from Research to Prevent Blindness, NY. Kendall Lyons has been supported by WSU Honors College Dean's Grant. The authors are grateful to AIM for the support and hospitality.

Data availability The data that support the findings of this study are available from the corresponding author. The Python packages employed in the study are described within the article.

Declarations

Conflict of interest Professor Giovanna Guidoboni would like to disclose that he received remuneration from Qlaris and Foresite Healthcare, serving as a consultant. All relationships listed above are pursuant to UMaine's policy on outside activities. Professor Alon Harris would like to disclose that he received remuneration from AdOM, Qlaris, and Cipla for serving as a consultant, and he serves on the board of AdOM, Qlaris, and SlitLed. Professor Alon Harris holds an ownership interest in AdOM, Oxymap, Qlaris, and SlitLed. All relationships listed above are pursuant to Icahn School of Medicine's policy on outside activities.

References

1. Hernandez, R.J., Roberts, P.A., El-Bouri, W.K.: Advancing treatment of retinal disease through in silico trials. Prog. Biomed. Eng. **5**(2), 022002 (2023). https://doi.org/10.1088/2516-1091/acc8a9
2. Harris, A., Guidoboni, G., Siesky, B., Mathew, S., Vercellin, A.C.V., Rowe, L., Arciero, J.: Ocular blood flow as a clinical observation: value, limitations and data analysis. Prog. Retin. Eye Res. **78**, 100841 (2020)
3. Puyo, L., Paques, M., Fink, M., Sahel, J.-A., Atlan, M.: Waveform analysis of human retinal and choroidal blood flow with laser doppler holography. Biomed. Opt. Express **10**(10), 4942–4963 (2019)
4. Julien, L., Bonnin, S., Paques, M., Fullana, J.-M.: One-dimensional modeling of microvascular hemodynamics in the retina using multimodal imaging. Phys. Fluids **35**(6) (2023)
5. Prud'homme, C., Sala, L., Szopos, M.: Uncertainty propagation and sensitivity analysis: results from the ocular mathematical virtual simulator. Math. Biosci. Eng. **18**(3), 2010–2032 (2021). https://doi.org/10.3934/mbe.2021105
6. Sala, L., Prud'homme, C., Guidoboni, G., Szopos, M., Harris, A.: Mathematical assessment of the role of three factors entangled in the development of glaucoma by means of the ocular mathematical virtual simulator. In: Vermolen, F.J., Vuik, C. (eds.) Numerical Mathematics and Advanced Applications ENUMATH 2019, pp. 851–860. Springer, Cham (2021)
7. Sala, L., Prud'homme, C., Guidoboni, G., Szopos, M., Harris, A.: The ocular mathematical virtual simulator: a validated multiscale model for hemodynamics and biomechanics in the human eye. Int. J. Numer. Methods in Biomed. Eng. (2024). https://doi.org/10.1002/cnm.3791
8. Carichino, L., Harris, A., Lapin, S., Guidoboni, G., Cassani, S., Silvestri, A.D., Tinelli, C., Milano, G., Siesky, B., Vercellin, A.C.V.: Waveform parameters of retrobulbar vessels in glaucoma patients with different demographics and disease severity. Eur. J. Ophthalmol. **30**(5), 1019–1027 (2020). https://doi.org/10.1177/1120672119848259. (**PMID: 31064210**)
9. Carichino, L., Guidoboni, G., Vercellin, A.V., Milano, G., Cutolo, C.A., Tinelli, C., Silvestri, A.D., Lapin, S., Gross, J.C., Siesky, B., Harris, A.: Computer-aided identification of novel ophthalmic artery waveform parameters in healthy subjects and glaucoma patients. Model. Artif. Intell. Ophthalmol. **1**(2), 59–59 (2016). https://doi.org/10.35119/maio.v1i2.31
10. https://opencv.org/. [Online; Accessed 31 Jan 2024]
11. https://numpy.org/. [Online; Accessed 31 Jan 2024]

12. Mohan, S.: Python OpenCV—image smoothing using averaging, Gaussian blur and median filter. https://machinelearningknowledge.ai/python-opencv-image-smoothing-using-averaging-gaussian-blur-and-median-filter/. [Online; Accessed 31 Jan 2024] (2021)
13. Guidoboni, G., Harris, A., Cassani, S., Arciero, J., Siesky, B., Amireskandari, A., Tobe, L., Egan, P., Januleviciene, I., Park, J.: Intraocular pressure, blood pressure, and retinal blood flow autoregulation: a mathematical model to clarify their relationship and clinical relevance. Investig. Ophthalmol. Vis. Sci. **55**(7), 4105–4118 (2014)
14. Pedley, T.J., Brook, B.S., Seymour, R.S.: Blood pressure and flow rate in the giraffe jugular vein. Philos. Trans. R. Soc. Lond. Ser. B Biol. Sci. **351**(1342), 855–866 (1996)
15. Guidoboni, G., Harris, A., Carichino, L., Arieli, Y., Siesky, B.A.: Effect of intraocular pressure on the hemodynamics of the central retinal artery: a mathematical model. Math. Biosci. Eng. **11**(3), 523–546 (2014)
16. https://scipy.org/. [Online; Accessed 31 Jan 2024]
17. Moore, N.A., Harris, A., Wentz, S., Vercellin, A.C.V., Parekh, P., Gross, J., Hussain, R.M., Thieme, C., Siesky, B.: Baseline retrobulbar blood flow is associated with both functional and structural glaucomatous progression after 4 years. Br. J. Ophthalmol. (2016)
18. Siesky, B., Wentz, S.M., Januleviciene, I., Kim, D.H., Burgett, K.M., Verticchio Vercellin, A.C., Rowe, L.W., Eckert, G.J., Harris, A.: Baseline structural characteristics of the optic nerve head and retinal nerve fiber layer are associated with progressive visual field loss in patients with open-angle glaucoma. PLoS ONE **15**(8), 0236819 (2020)
19. Dorner, G.T., Polska, E., Garhöfer, G., Zawinka, C., Frank, B., Schmetterer, L.: Calculation of the diameter of the central retinal artery from noninvasive measurements in humans. Curr. Eye Res. **25**(6), 341–345 (2002)
20. Riva, C.E., Feke, G.T., Eberli, B., Benary, V.: Bidirectional LDV system for absolute measurement of blood speed in retinal vessels. Appl. Opt. **18**(13), 2301–2306 (1979)
21. Guidoboni, G., Harris, A., Sacco, R.: Mathematical Modeling of Ocular Fluid Dynamics: From Theory to Clinical Applications. Modeling and Simulation in Science, Engineering, and Technology, Springer, Berlin (2019)
22. Kantorovich, L.V.: Mathematical methods of organizing and planning production. Manag. Sci. **6**(4), 366–422 (1960)
23. Harris, A., Topouzis, F., Wilson, M.R., Founti, P., Kheradiya, N.S., Anastasopoulos, E., Gong, G., Yu, F., Jonescu-Cuypers, C.P., Pappas, T., et al.: Association of the optic disc structure with the use of antihypertensive medications: the Thessaloniki eye study. J. Glaucoma **22**(7), 526–531 (2013)
24. Wurster, P., Harris, A., Gonzalez, A.C., Adjei, S., Vercellin, A.V., Mathew, S., Lang, M., Eikenberry, J., Siesky, B.: Risk factors for open-angle glaucoma in persons of Latin American descent. J. Glaucoma **29**(3), 217–225 (2020)
25. Guidoboni, G., Nunez, R., Keller, J., Wikle, C., Robinson, E., Verticchio, A., Siesky, B., Oddone, F., Quaranta, L., Wirostko, B., et al.: Precision medicine and glaucoma management: how mathematical modeling and artificial intelligence help in clinical practice. Expert Rev. Ophthalmol. **17**(5), 299–301 (2022)
26. Harris, A., Vercellin, A.V., Weinreb, R.N., Khawaja, A., MacGregor, S., Pasquale, L.R.: Lessons from the glaucoma foundation think tank 2023: a patient-centric approach to glaucoma. J. Glaucoma 10–1097 (2023)